OPEN ACCESS



Transient LoBALs at High Velocities: A Case of Extreme Broad Absorption Line Variability in J115636.82+085628.9*

P. Aromal^{1,2}, R. Srianand³, S. C. Gallagher^{1,2}, M. Vivek⁴, and P. Petitjean⁵

Physics and Astronomy Department, University of Western Ontario, 1151 Richmond Street, London, N6A 3K7, Ontario, Canada; apathaya@uwo.ca

Institute for Earth and Space Exploration, Western University, 1151 Richmond Street, London, ON N6A 3K7, Canada

IUCAA, Postbag 4, Ganeshkind, Pune 411007, India

Indian Institute of Astrophysics, Bangalore 560034, India

Institut d'Astrophysique de Paris, Sorbonne Université and CNRS, 98bis boulevard Arago, 75014 Paris, France

Received 2025 June 3; revised 2025 July 7; accepted 2025 July 25; published 2025 September 4

Abstract

We present a multiepoch spectroscopic study of the broad absorption line (BAL) quasar J115636.82+085628.9 ($z_{\rm em}=2.1077$), based on five spectra spanning nearly two decades in the observer's frame. This source exhibits remarkable variability in both low-ionization (LoBAL: Al III and Mg II) and high-ionization (HiBAL: C IV and Si IV) absorption features. For the first time, we detect the emergence and subsequent disappearance of LoBAL troughs at high velocities ($\sim 20,000~{\rm km~s^{-1}}$), coinciding with the strengthening and weakening of the corresponding HiBAL absorption. The C IV BAL profile extends from $\sim 6700~{\rm km~s^{-1}}$ to a conservative upper limit of 30,000 km s⁻¹ and is composed of narrow, variable absorption features embedded within a broad, smooth envelope. Both C IV and Si IV BAL troughs exhibit dramatic equivalent width (EW) changes—among the most extreme reported to date. Notably, these EW variations are strongly anticorrelated with continuum flux changes inferred from optical photometric light curves. We interpret this variability as the result of a new absorbing flow transiting into our line of sight, increasing the shielding of a more distant, preexisting outflow and giving rise to transient LoBAL absorption. This scenario supports a unified picture in which LoBAL and HiBAL features arise from similar outflow structures, with observed differences governed primarily by line-of-sight column densities consistent with previous findings.

Unified Astronomy Thesaurus concepts: Quasars (1319)

1. Introduction

Strong outflows from quasars manifest themselves as broad absorption lines (BALs) having widths of several 1000 km s and outflow velocities reaching up to several 10,000 km s⁻¹ with respect to the systemic redshift (zem) of the quasars. About 10%-20% of all optically selected quasars show BALs (R. J. Weymann et al. 1991), and this fraction can reach 40% if dust and other observational biases are properly taken into account (X. Dai et al. 2008; J. T. Allen et al. 2011). These outflows are believed to be related to accretion disk winds (e.g., N. Murray et al. 1995) and have sufficient mechanical energy and momentum to provide significant feedback to the gas in galaxies (e.g., N. Arav et al. 2018). Also, recent studies provide growing evidence that BAL and non-BAL quasars exhibit similar distributions in emission-line outflow and physical properties, suggesting that they are drawn from the same parent population (A. L. Rankine et al. 2020; H. Ahmed et al. 2024; M. J. Temple et al. 2024).

BAL quasars are mainly divided into two main subtypes: (1) high-ionization BAL (HiBAL) sources that show absorption produced by highly ionized species such as C IV, Si IV, N V, etc., and (2) low-ionization BAL (LoBAL) sources where we

Original content from this work may be used under the terms of the Creative Commons Attribution 4.0 licence. Any further distribution of this work must maintain attribution to the author(s) and the title of the work, journal citation and DOI.

see absorption from low-ionized species such as Al III, Fe II, and Mg II, etc. The time variability in both HiBALs and LoBALs serves as a crucial tool for probing the nature, origin, and evolution of quasar outflows (R. Srianand & P. Petitjean 2001; R. R. Gibson et al. 2008, 2010; D. M. Capellupo et al. 2011; N. Filiz Ak et al. 2012; M. Vivek et al. 2014; D. De Cicco et al. 2018; W.-J. Lu & Y.-R. Lin 2020; P. Aromal et al. 2022, 2024). Time-resolved studies of BAL profiles, both in LoBALs and HiBALs, have provided significant insights into the physical conditions, ionization states, covering fractions, and spatial locations of these outflows relative to the central source (for example, see D. M. Capellupo et al. 2012; N. Arav et al. 2018; K. S. Green et al. 2023). Monitoring BAL variability across different timescales provides stringent constraints on the lifetime and dynamics of the outflows, shedding light on the underlying physical mechanisms driving them. In particular, extreme cases of variability, such as sudden emergence, complete disappearance, or kinematic changes of BAL troughs, are of particular interest, as they offer valuable clues about the complex nature of quasar winds (E. Y. Vilkoviskij & M. J. Irwin 2001; N. Filiz Ak et al. 2013; S. M. McGraw et al. 2017; D. De Cicco et al. 2018; J. A. Rogerson et al. 2018; M. Vivek et al. 2018; W.-J. Lu & Y.-R. Lin 2025). Such significant changes, often observed over rest-frame timescales of months to years (e.g., N. Filiz Ak et al. 2013; M. Vivek et al. 2014), are typically attributed to fluctuations in the quasar's ionizing flux and/or variations in the outflow's covering fraction, or transverse bulk motion within the outflow. In addition, it was also shown that changes in shielding gas column density originating from highly ionized outflows close to the accretion disk can lead to

^{*} Based on observations collected at Southern African Large Telescope (SALT; Programme IDs 2015-1-SCI-005, 2018-1-SCI-009, 2019-1-SCI-019, and 2020-1-SCI-011) and the European Organisation for Astronomical Research in the Southern Hemisphere under ESO programme 093.A-0255.

ionization changes in outflows located further away, as demonstrated in the case of NGC 5548 (J. S. Kaastra et al. 2014; N. Arav et al. 2015). This mechanism becomes important when one sees highly correlated variability over the full absorption profile when there is no appreciable change in the optical continuum flux. Hence, it is important to follow up BAL sources that show extreme BAL variability over restframe timescales of a few months to give us an opportunity to constrain the nature of these outflows (M. Vivek et al. 2018; P. Aromal et al. 2021) that are crucial in active galactic nucleus feedback-galaxy evolution models.

In the literature, many studies have found interesting LoBALs which have shown appearance or disappearance signatures (M. Vivek et al. 2012; N. Filiz Ak et al. 2014; W. Yi et al. 2019; W. Yi & J. Timlin 2021) and, in some cases, even kinematic shifts (W.-J. Lu & Y.-R. Lin 2020). However, it is important to note that this extreme variability is very rare in LoBALs compared to their HiBAL counterparts (W. Yi & J. Timlin 2021). Also, it was shown that LoBALs tend to be seen at lower velocities relative to corresponding HiBALs like C IV that reach very high velocities of a few 10,000 km s⁻¹ (N. Filiz Ak et al. 2014). F. Hamann et al. (2019) concluded that LoBALs form in harsh radiative environments, characterized by high-ionization parameters (U) similar to HiBALs, but with significantly larger total column densities that enhance radiative shielding. Using the spectral synthesis modeling software SimBAL, it has been shown that several LoBALs, particularly FeLoBALs, possess large total column densities $(\log(N_{\rm H})$ up to 23), and span a wide range of ionization parameters and gas densities (K. M. Leighly et al. 2018; H. Choi et al. 2022). Interestingly, from an evolutionary picture, some studies interpret LoBALs as part of a short-lived stage in quasar evolution where the SMBH is evacuating large amounts of gas from its circumnuclear environment, otherwise known as the "blowout" phase (T. Urrutia et al. 2009).

We have been undertaking a dedicated spectroscopic monitoring of 64 HiBALs showing high-velocity (ejection velocities in excess of 15,000 km s⁻¹) outflows using Southern African Large Telescope (SALT; P. Aromal et al. 2023, 2024). This, combined with the Sloan Digital Sky Survey (SDSS) spectra, allows us to probe time variability over a few months to \sim 8 yr in the quasar's rest frame. Here we study one of the interesting BAL quasars (J115636.82+085628.9 hereafter J1156+0856, $z_{em} = 2.1077$) in our sample that shows the maximum C IV BAL equivalent width (EW) variability that coincides with an episode of strong photometric light curve variations. The quasar has a bolometric luminosity of $log(L_{bol}[erg\ s^{-1}]) = 46.75$ and a black hole mass of $\log(M_{\rm BH}/M_{\odot}) = 8.92$, both of which are within the typical range of quasar properties in our sample (P. Aromal et al. 2023). This source is also unique in that we observe both the emergence of LoBALs in Al III and Mg II, and their subsequent disappearance during our monitoring (effectively a HiBAL-LoBAL-HiBAL transition), which is an extremely rare occurrence. This LoBAL absorption emerges at high velocities of $20,000 \,\mathrm{km \, s^{-1}}$ ($\sim 0.07c$) and such cases have not been previously reported in the literature. We find that the LoBAL variability is closely associated with HiBAL variations as seen in C IV and Si IV BALs. Such variability is rare in nature and offers us a unique opportunity to study the origin of LoBALs and their connection to their HiBAL counterparts. It will also help us in understanding what triggers BAL variations, as

these different ionized species may come from different parts of the outflow, which may respond differently to any global mechanism that leads to these variations.

The paper is organized as follows. In Section 2, we present the observations used in our study. Section 3 provides details of results based on the absorption line variability in J1156 +0856. Section 4 presents the discussions, and in Section 5, we discuss the main results and provide a summary of our work. Throughout this paper we use the flat Λ CDM cosmology with $H_0 = 70 \, \mathrm{km \, s}^{-1} \, \mathrm{Mpc}^{-1}$ and $\Omega_{m,0} = 0.3$.

2. Observations and Data Used in This Study

We obtained two high-quality, fully reduced spectra of J1156+0856 from SDSS/Baryon Oscillation Spectroscopic Survey (BOSS) archives, data release 16 (B. W. Lyke et al. 2020). The SDSS (BOSS) spectra cover a wavelength range of 3800–9200 (3600–10400) Å at a resolution, $R \sim 2000$ (150 km s⁻¹). Using the SALT, we carried out spectral monitoring of J1156 + 0856 from 2022-2024 and obtained three spectra with almost 1 yr of separation in the observed frame. For this, we used the Robert Stobie Spectrograph (RSS, E. B. Burgh et al. 2003; H. A. Kobulnicky et al. 2003) at SALT in long-slit mode using a 1.5 wide slit and the PG0900 grating. For grating angle = 14.375, this setting provides a spectrum with wavelength coverage of 3900–7000 Å, excluding the two CCD gap regions at 4935-5000 Å and 5980-6050 Å. Details of all available spectra are given in Table 1. The shortest and longest timescale probed at the quasar's rest frame are 0.28 and 6.7 yr, respectively.

Continuum fitting of the observed spectra is very important in BAL variability studies. We used the publicly available multicomponent spectral fitting code PYQSOFIT (H. Guo et al. 2018) to fit the continuum and broad emission lines (BEL) in our spectra. We identified wavelength ranges devoid of any absorption lines and then fitted these regions with a power-law + multiple Gaussian (for BELs) model, which provided fairly good fits using χ^2 minimization as shown in Figure 1.

We also characterize the continuum variability of the source using broadband photometric light curves. For this, we obtained publicly available light curves of J1156+0856 from the Panoramic Survey Telescope and Rapid Response System (Pan-STARRS; K. C. Chambers et al. 2016), the Palomar Transient Factory (N. M. Law et al. 2009), and the Zwicky Transient Facility (ZTF; E. C. Bellm et al. 2019a, 2019b) surveys. Pan-STARRS data includes five broadband filters, i.e., g, r, i, z, and y, whereas ZTF uses the g, r, and i bands. Details of the photometric variability of J1156+0856 are discussed in Section 3.3.

3. Absorption Line Variability

Figure 1 shows the spectra of J1156+0856 obtained during five different epochs (shown in blue lines) together with the best-fit continuum (shown in red lines). In addition, the continuum-normalized spectra covering the C IV and Si IV absorption are compared in Figure 2. The details of C IV absorption line-based measurements are provided in Table 2. As mentioned above, the spectra from the initial two epochs (shown in the top two panels) are from SDSS, and the spectra

⁶ https://github.com/legolason/PyQSOFit

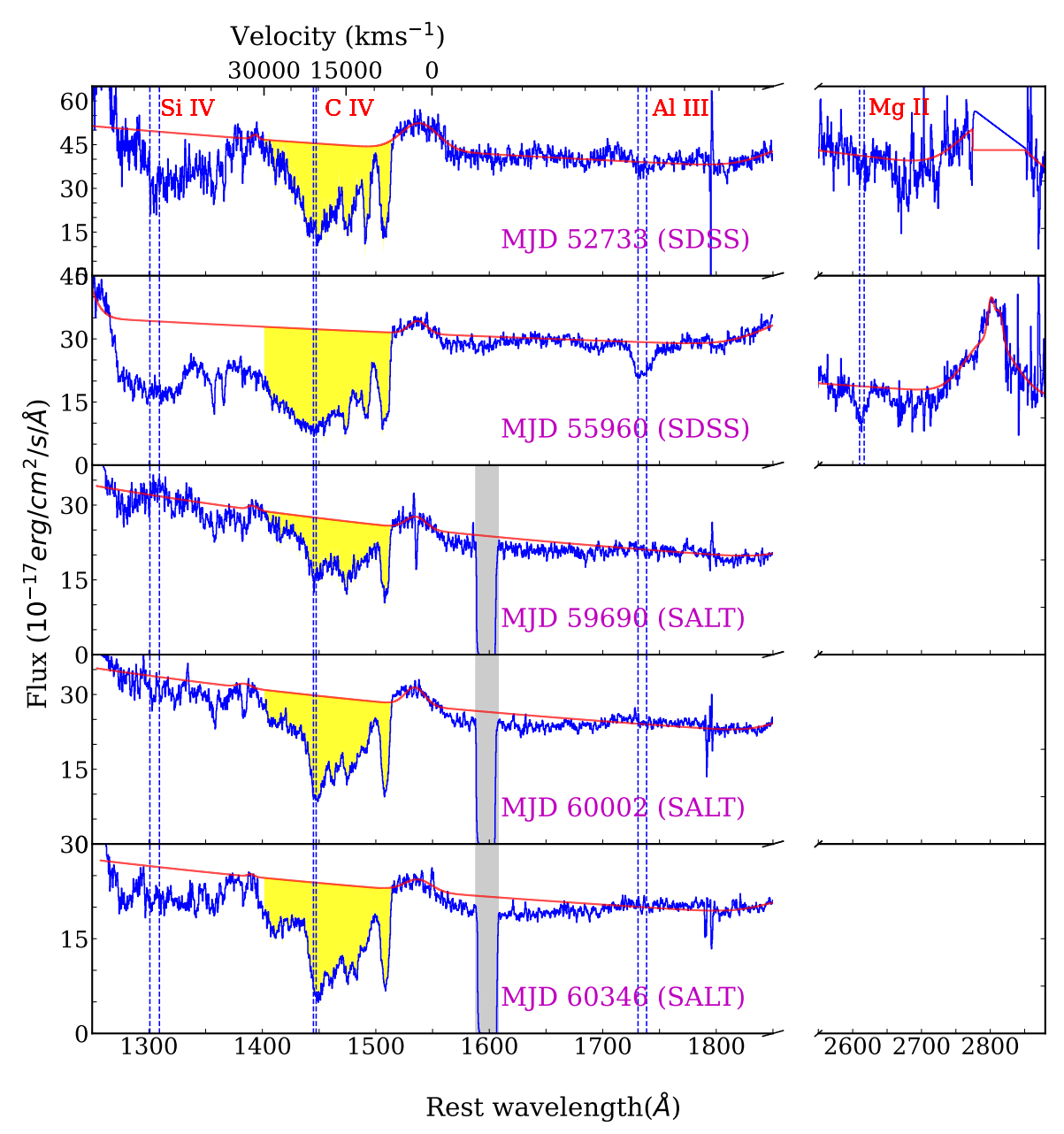


Figure 1. The rest-frame spectra of J1156+0856 (blue), along with the best continuum fit (red), defined with respect to $z_{\rm em}$ = 2.1077 are shown. Absorption line variability of C IV broad components (up to $v = 30,000~{\rm km~s}^{-1}$) identified with yellow-shaded regions is apparent. The velocity scale for C IV BAL absorption with respect to the systemic redshift ($z_{\rm em}$ = 2.1077) is provided at the top. The blue dashed lines represent the absorption in different ionized species for BAL component "D" ($v \sim 20,000~{\rm km~s}^{-1}$), where LoBAL absorption emerges during epoch 2 (refer to Section 3.1). Gray-shaded regions represent the CCD gaps in SALT spectra.

 Table 1

 Log of Observations and Details of Spectra Obtained at Different Epochs

| Epoch | Telescope | Date of observations | | $\Delta t_{ m rest}^{}$ | Exposure Time | Spectral Res. | Wavelength Range | S/N ^b |
|-------|-----------|----------------------|-------|-------------------------|---------------|---------------|------------------|------------------|
| | | (M/D/Y) | (MJD) | (yr) | (s) | $(km s^{-1})$ | (Å) | |
| 1 | SDSS | 04/04/2003 | 52733 | | 2340 | 150 | 3808-9212 | 11.32 |
| 2 | SDSS | 02/03/2012 | 55960 | 2.84 | 3603 | 150 | 3555-10344 | 17.79 |
| 3 | SALT | 04/21/2022 | 59690 | 6.13 | 2300 | 304 | 3897-6980 | 17.64 |
| 4 | SALT | 02/27/2023 | 60002 | 6.40 | 2400 | 304 | 3897-6980 | 26.45 |
| 5 | SALT | 02/06/2024 | 60346 | 6.71 | 2400 | 304 | 3907-6984 | 26.14 |

Notes

^a Time difference between spectroscopic epochs in the rest frame with respect to the first epoch.

 $^{^{\}rm b}$ Signal-to-noise ratio per pixel calculated over the wavelength range 5000–5200 Å.

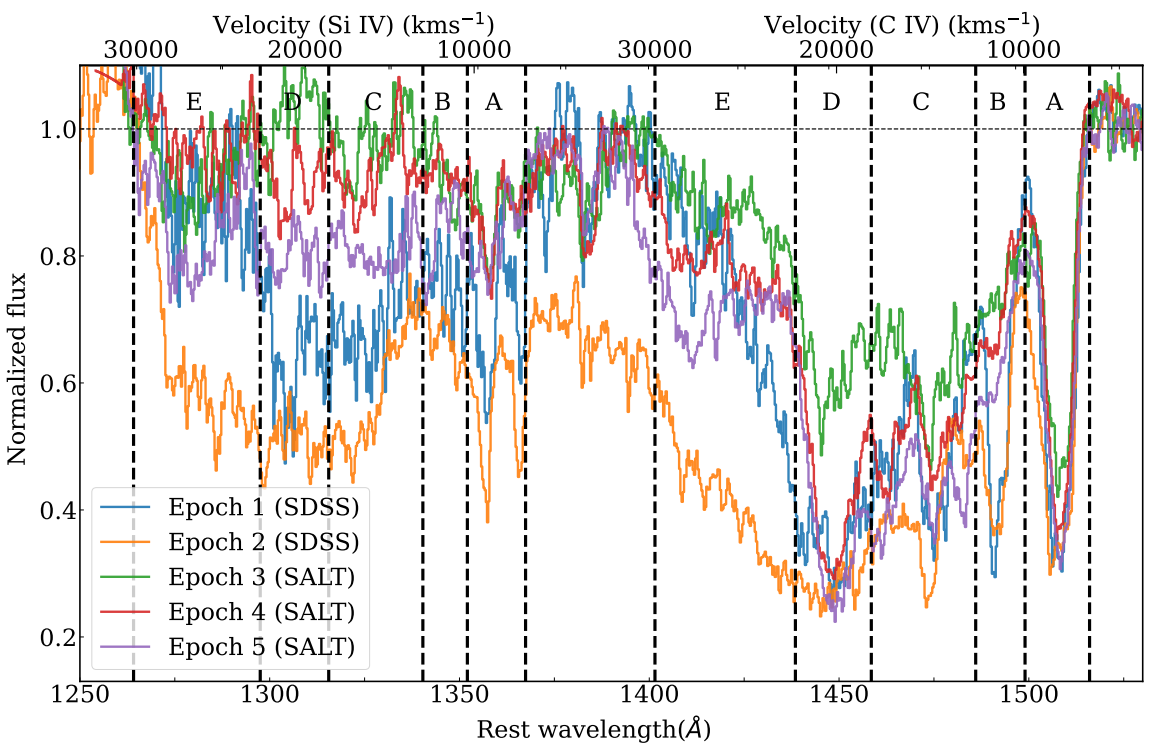


Figure 2. The figure shows the overlaid normalized spectra of J1156+0856 in the five epochs, focusing on regions blueward of C IV BEL that cover C IV and Si IV BAL regions. The black dashed lines indicate the distinct BAL regions for Si IV (left) and C IV (right), as described in Section 3.1.

| Table 2 | | | | | | | | |
|-------------------|--------|------------|----|-----------|--------|--|--|--|
| Log of Equivalent | Widths | Calculated | at | Different | Epochs | | | |

| Epoch | $W_{\c C_{\circ}\ IV} \ (A)$ | $\frac{\frac{dW_{\text{C IV}}}{a}}{(\mathring{A} \overset{dt}{yr}^{-1})}$ | $W_{\text{C,IV}}^{\text{A}}{}^{\text{b}}$ (A) | $W_{\text{C,IV}}^{\text{B}}$ (A) | $W^{\mathrm{C}}_{\mathrm{C,IV}}{}^{\mathbf{b}}$ (A) | $W^{\mathrm{D}}}\mathrm$ | $W_{\text{C,IV}}^{\text{E}}^{\text{b}}$ (A) |
|-------|------------------------------|---|---|----------------------------------|---|--|---|
| 1 | 47.11 ± 0.60 | ••• | 6.37 ± 0.20 | 5.14 ± 0.18 | 13.54 ± 0.28 | 12.66 ± 0.23 | 9.38 ± 0.39 |
| 2 | 65.16 ± 0.29 | 6.34 | 7.43 ± 0.11 | 6.03 ± 0.09 | 16.25 ± 0.14 | 14.04 ± 0.11 | 21.39 ± 0.18 |
| 3 | 30.43 ± 0.35 | -10.56 | 4.93 ± 0.12 | 3.20 ± 0.12 | 10.26 ± 0.17 | 7.38 ± 0.15 | 4.65 ± 0.20 |
| 4 | 41.18 ± 0.23 | 39.07 | 5.40 ± 0.08 | 3.41 ± 0.08 | 13.12 ± 0.11 | 11.23 ± 0.09 | 8.00 ± 0.14 |
| 5 | 49.33 ± 0.25 | 26.87 | 6.23 ± 0.09 | 4.32 ± 0.08 | 15.51 ± 0.11 | 12.66 ± 0.10 | 10.60 ± 0.15 |

Notes

for the subsequent three epochs were obtained using SALT. The C IV BAL (yellow-shaded region in each panel) in J1156 +0856 spans a velocity range that starts at $v_{\rm min} \sim 6700~{\rm km~s}^{-1}$ and extends up to the conservative upper limit of 30,000 km s $^{-1}$. This is according to the definition given in R. J. Weymann et al. (1991), where a BAL is defined as a continuous absorption wider than 2000 km s $^{-1}$ below 90% of the continuum level. There is a strong possibility that absorption is present at even higher velocities than this limit (especially during the second epoch), but for the ease of discussions and to avoid possible overlap with Si IV absorption, we set the maximum BAL velocity $v_{\rm max}$ to 30,000 km s $^{-1}$ in our analysis. The main trends we observe from Figure 2 are,

1. The C IV BAL region is extremely variable and undergoes nonuniform depth variations between any pair of

- spectroscopic epochs considered. This is confirmed by the rest EW variations from column (2) in Table 2.
- 2. The C IV absorption is strongest (i.e., with a rest EW of 65.16 ± 0.29 Å) during epoch 2 (i.e., MJD 55960). During this epoch, we also see strong, broad, and saturated Si IV absorption. A narrow Al III and Mg II absorption with the ejection velocity of 18,000–23,000 km s⁻¹ and 19,000–22,500 km s⁻¹ respectively that coincides with the velocity range where deepest C IV absorption is present. This component is identified with the vertical blue dashed lines in Figure 1.
- 3. The Si IV absorption observed during epoch 2 is broad with a flat-bottomed profile, indicative of line saturation and a covering factor of $f_c \sim 0.5$. Here, we assume that the absorption depth of the saturated Si IV BAL in the continuum-normalized spectrum corresponds to its

a $\frac{dW_{C IV}}{dt}$ is the rate of change of equivalent width of the entire BAL region (including A, B, C, D, and E components) with respect to the previous epoch in rest-frame timescale.

^b W_{CIV}^A , W_{CIV}^B , W_{CIV}^C , W_{CIV}^C , and W_{CIV}^E are the C IV rest equivalent width of region A, B, C, D, and E, respectively, integrated over a distinct portion of the absorption profile.

- covering fraction. However, the C IV absorption depth is higher than that of Si IV, suggesting a covering factor of Si IV being smaller than that of C IV.
- 4. The C IV absorption is at its weakest strength (i.e., rest EW of $30.43\pm0.35\,\text{Å}$) during epoch 3 (i.e., MJD 59690), and Si IV and Al III absorption lines are not detected in this epoch. Unfortunately, the wavelength range of Mg II absorption is not covered by our SALT observations. It is also evident from Figure 2 that some of the narrow C IV absorption components clearly visible during epoch 1 and epoch 2 are not visible in the spectrum taken during epoch 3.
- 5. The C IV absorption shows an increasing trend in the following two epochs, i.e., epochs 4 and 5. The overall profile looks roughly similar (compared to epoch 1) except for a distinct component emerging around an ejection velocity of 25,000–30,000 km s⁻¹. However, some of the narrow components seen in the first two epochs do not reappear during this period.

Thus, the variability of the C IV absorption line shows interesting trends. To gain further insight, we next study the variability of the absorption strength as a function of the outflow velocity. For this, we adopt a method where we divide the entire BAL profile into a few specific regions of interest based on the overall variability and study them in detail in Sections 3.1–3.3.

3.1. Broad Absorption Line Regions

We split the entire C IV BAL profile, as observed in epoch 1, into five regions after carefully considering the diverse nature of profile variability during our monitoring. The velocity ranges for regions A, B, C, D, and E are 6700–10,000 km s $^{-1}$, 10,000–12,500 km s $^{-1}$, 12,500–18,000 km s $^{-1}$, 18,000–22,000 km s $^{-1}$, and 22,000–30,000 km s $^{-1}$, respectively, as shown for both the C IV and Si IV absorption in Figure 2. Again, these regions are chosen keeping in mind the interesting variability shown at subsequent epochs.

Now, let us look at the BAL profile observed in the first epoch (see Figure 2). Both regions A and B consist of a strong, narrow component with a distinct absorption profile in the first epoch. We detect corresponding Si IV doublets for region A, whereas region B lacks the same despite having a comparable C IV absorption depth. This may indicate the overall column density of gas contributing to A being much larger than that of B. The C IV absorption strength, being equal, can be related to line saturation combined with partial coverage. In region C, multiple C IV narrow components are visible in the first epoch, and they show extreme variability in both their position and profile shape in subsequent epochs, as discussed later in detail. Region D consists of the strongest distinct C IV absorption with a possible unresolved Si IV absorption present at the corresponding velocities. Region E, which is at the highest velocities, does not have any distinct absorption components, but a smooth absorption is present throughout the region, which gradually decreases in strength toward the high-velocity end. Now, let us look at the variability in each defined BAL region and study in detail the nature of the BAL outflow in J1156+0856.

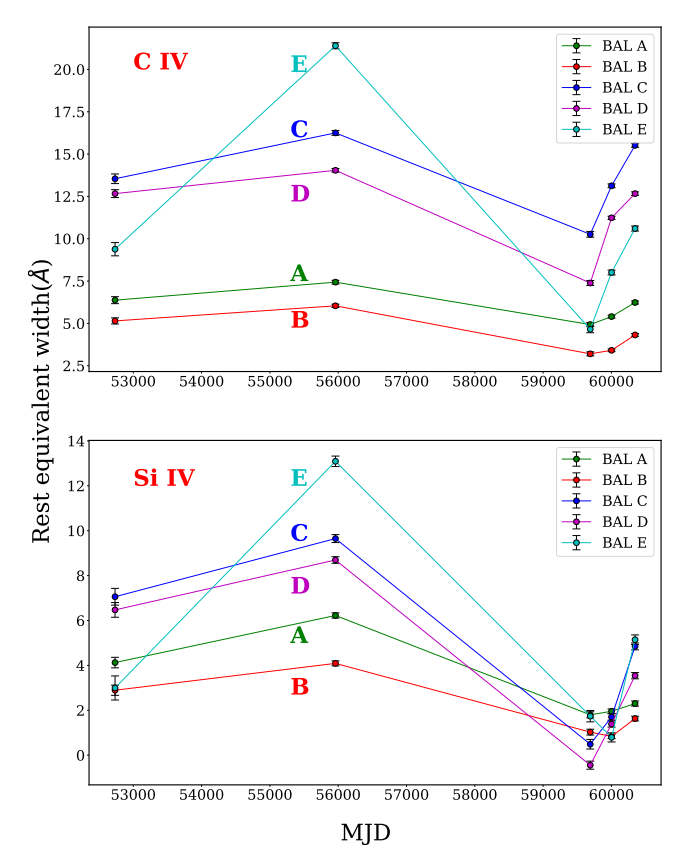


Figure 3. This figure shows the C IV and Si IV equivalent widths calculated for different BAL regions as defined in Section 3.1 as a function of time.

3.2. Equivalent Width Variations

In terms of the variations of the equivalent width (W), J1156 +0856 shows one of the most extreme changes in absorption strength ever reported in BAL quasars. Interestingly, these variations are not uniform across the BAL profile, and analyzing variability in different BAL regions helps reveal a clear picture of its unique nature. Figure 2 shows the interesting depth variations in each BAL region, and Figure 3 and Table 2 show the EWs calculated for each BAL region (as defined in Section 3.1) at different epochs. Now, we analyze the BAL variability in detail in the following paragraphs.

We described the BAL profile in epoch 1 in the previous Section 3.1. In the second SDSS epoch (\sim 3 yr in rest frame after epoch 1), we see a large positive change in the equivalent width $(\Delta W \sim 18 \text{ Å})$, especially at velocities greater than 20,000 km s⁻¹. In this epoch, regions A and B show little variation in C IV, although corresponding Si IV absorption has increased considerably. However, caution should be exercised for these regions since possible C IV absorption exceeding 30,000 km s⁻¹ can overlap with Si IV absorption and lead to higher values of Si IV EW. Region C shows a large variation with the emergence of a narrow component at 13,000 km s⁻¹ whereas an already existing absorption component at 15,000 km s⁻¹ becomes narrower and deeper. The regions D and E show significant depth variations, where E shows an increase in depth as large as ~ 0.5 at $\sim 25,000 \,\mathrm{km \, s^{-1}}$. Interestingly, for region D, in addition to Si IV absorption becoming deeper, a considerable Al III and Mg II absorption also emerges at \sim 18,000–22,000 km s⁻¹. The EWs of the new

Al III and Mg II absorption are $4.77 \pm 0.16 \,\text{Å}$ and 2.63 ± 0.24 Å, respectively. It is interesting to note that the low-ionization absorption emerges in a narrow region at relatively large velocities. This is opposite to what we expect based on studies such as N. Filiz Ak et al. (2014), which found that the Al III BALs generally correspond to the low-velocity portions of the C IV trough. Also, there is little difference in the peak absorption depth (at $v \sim 20,000 \,\mathrm{km \, s^{-1}}$) in region D between epochs 1 and 2, despite the emergence of LoBALs at corresponding velocities, indicating the strong saturation in C IV absorption. The region E shows the strongest variations $(\Delta W \sim 12 \text{ Å})$ with significant changes in depth accompanied by a strong Si IV absorption appearing at these velocities for the first time during our monitoring. These variations point toward a possibly large increase in the line-of-sight (LOS) column density across the entire profile during epoch 2. This can be associated with the eruption of a strong high-velocity wind from the accretion disk as implied by the large velocity gradient of this new absorption or the transit of a dense flow component into our LOS at relatively smaller distances, as discussed later in Section 4.

Epoch 3 using SALT is observed after another \sim 3 yr in the rest frame since epoch 2. Once again, we observe dramatic changes in the absorption, but this time the entire BAL weakens significantly ($\Delta W \sim -35 \, \text{Å}$) and reaches the lowest EW observed. Region A shows the least depth variations, confirming its highly saturated nature. But the resolved Si IV doublet from region A weakens and also reaches a doublet ratio close to 2:1, indicating the Si IV absorption may have become optically thin in this epoch. More interestingly, the distinct C IV narrow component in region B completely disappears. Both C and D show a large decrease in C IV and Si IV depth, with distinct narrow components in these regions almost disappearing. It is interesting to note that this also leads to the complete disappearance of Al III absorption at \sim 20,000 km s⁻¹. We are unable to comment on the further evolution of Mg II absorption in this study as the SALT spectra do not cover this wavelength region. Region E also undergoes a significant weakening and reaches depths (~ 0.15) smaller than those of epoch 1. Overall these variations contribute to one of the highest changes in C IV BAL EW (\sim 35 Å) reported in the literature (see Figure 13 of N. Filiz Ak et al. 2013, where the highest absolute EW changes are $\sim 15 \,\text{Å}$ in one of the largest BAL quasar samples).

In epoch 4, followed by epoch 5, the BAL again goes through a strengthening episode ($\Delta W \sim 8 \,\text{Å}$), albeit not as dramatic as the one observed in epoch 2. It is interesting to note that this change occurs on relatively short timescales of a few months in the rest frame, thanks to our close monitoring using SALT. The BAL EW increases considerably with one of the largest rates of change of EWs (\sim 39 Å yr⁻¹ between epoch 3 and 4 in rest-frame timescales, see Table 2 and Figure 3). In these later epochs, the absorption profile roughly becomes similar to that in epoch 1 except for (1) the C IV narrow component in region B does not reemerge despite small changes in the overall average depth, (2) the narrow components in region C undergo significant variability with possible kinematic shift signatures (3) the width of the broad component in region D decreases considerably while retaining roughly the same absorption depth at $v \sim 20,000 \text{ km s}^{-1}$ as in epoch 1. However, it is interesting to note that the Al III absorption present in epoch 2 never reappears, and (4) In

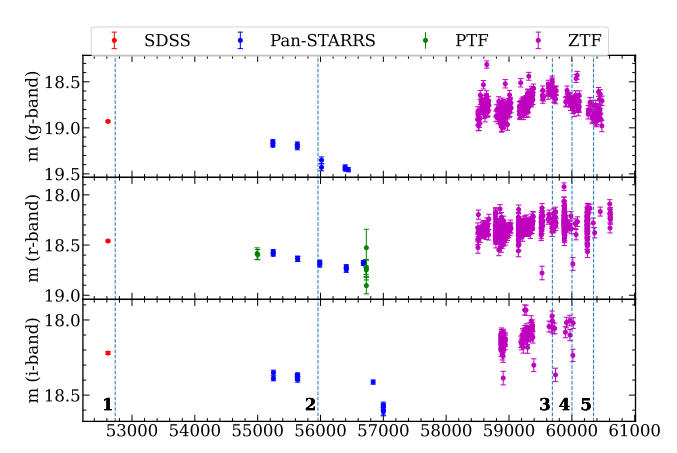


Figure 4. The light curves of J1156+0856 in g (top), r (middle), and i (bottom) optical bands are shown as obtained from publicly available photometric surveys. The spectroscopic epochs are marked (vertical blue dashed lines) with the epoch numbers marked in the bottom panel.

region E, a new absorption component emerges at 25,000–30,000 km s⁻¹ in epoch 4, which subsequently becomes stronger in epoch 5. The restoration of the overall absorption profile after a strengthening and weakening episode suggests that an absorber component may always be present along our LOS, possibly varying in its ionization structure. This suggests that the relative distribution of C IV absorber column density as a function of velocity remains roughly similar in the first and last epochs, despite the appearance of strong absorption between epochs 1 and 2. That said, the relatively minor changes in the absorption profile between these epochs are likely due to residual wind components that persist even after the disappearance of a large-scale outflow component from our LOS. We discuss the possible reasons for these variations in Section 4.

3.3. Light Curve Variations and Their Connection to Broad Absorption Line Variability

In Figure 4, we show the available light curves of J1156 +0856 obtained in three different filters (g, r, and i bands). These light curves are not sampled uniformly in time, but the ZTF measurements provide good coverage during our last three spectroscopic epochs. We find significant variations in the photometric magnitudes in all bands between our spectroscopic epochs, as shown in Figure 4. We ignore the relatively minor differences in filter transmission functions between surveys when comparing magnitudes in our analysis. This approach is justified by findings that the mean offsets in g- and r-band magnitudes between SDSS, Pan-STARRS, and ZTF are ~ 0.05 mag at the redshift of J1156+0856 (see Figure 1, L. Wu et al. 2024), which is negligible compared to the large magnitude variations observed in our source and does not impact any of our conclusions.

In epoch 2, as stronger absorption emerges, the source becomes dimmer by \sim 0.5 (\sim 0.3) mag in the g (r) band compared to epoch 1. Subsequently, the ZTF points close to epoch 3 show a significant brightening of the order of \sim 1 mag and \sim 0.5 mag in the g and r bands, respectively, as the BAL weakens. Although these changes are consistent with the BAL variability (in the g band), the decrease in depth of the BAL alone cannot account for such large variations in magnitudes observed. After epoch 3, we notice a gradual dimming in the g band (the same is not evident in the r band) until epoch 4.

These trends indicate that the absorbing gas may be responding to the changes in continuum flux, and an increase in continuum leads to the weakening of BAL features. This anticorrelation trend has been extensively reported in the literature (T. Wang et al. 2015; M. Vivek 2019; S. Mishra et al. 2021). This would suggest that in the case of J1156 +0856, photoionization-induced variations are important to explain the BAL variability. However, it is good to keep in mind that the changes in UV flux (as probed by the g band) and high-energy X-ray radiation, which can affect the ionization levels in the cloud, need not be correlated with each other (see, for example, N. Arav et al. 2015). This prevents us from drawing any serious conclusions with just UV/optical light curves in the absence of X-ray observations. In Section 4, we model the variations by combining spectral and photometric variations with photoionization simulations.

4. Discussions

4.1. The Appearance of a New Outflow Component?

One of the primary drivers of BAL variability is the change in the ionization structure of the outflow, induced by fluctuations in the ionizing flux incident on the absorber (C. J. Grier et al. 2015; P. Aromal et al. 2022). Alternatively, variability can result from changes in the covering fraction as the outflow transits our LOS or due to its bulk motion away from the accretion disk (D. M. Capellupo et al. 2013; S. M. McGraw et al. 2015; K. S. Green et al. 2023). Previous studies suggest that the underlying causes are often more complex, with both ionization changes and geometric effects contributing to the observed variability in many quasars (S. M. McGraw et al. 2017; P. Aromal et al. 2021).

Another plausible scenario, which is less explored, involves the presence of multiple outflow components, either located at varying distances from the disk or as distinct regions within the same outflow, separated on larger spatial scales. In such cases, the observed variability may depend on interactions between these different flow components (see, for example, N. Arav et al. 2015). In this study, we explore this multicomponent outflow scenario for J1156+0856 and argue that it provides a more comprehensive explanation for the observed variability than a simple photoionization-driven model involving a single outflowing cloud. While our analysis does not rule out the alternative mechanisms, we propose that this new picture—motivated by several intriguing observational features of J1156 + 0856—provides an equally viable explanation that aligns well with previous findings.

First, we consider either the emergence of a new outflow from the accretion disk or the transit of a strong outflow component into our LOS at a relatively smaller distance, which can lead to several interesting consequences for variability in a BAL outflow that is already present. The newly entered flow material can produce C IV absorption in favorable conditions and also significantly affect the ionization structure of a previously existing outflow at larger distances due to efficient shielding (see, for example, K. Fukumura et al. 2024). Effective shielding of ionizing radiation by this gas can prevent high-energy photons from reaching distant clouds, which can lead to an increase in the fraction of low-ionized species such as Al III and Mg II. Here, the variability will be difficult to explain as the two effects, i.e., the addition of a new absorbing material along our LOS and the possible changes in

the ionization structure of already existing outflows, play an important role in determining changes in the optical depth of various ionized species. Previous studies, such as M. Vivek et al. (2018), have shown that the column density ratios in BAL absorbers are highly sensitive to the shielding gas column density using CLOUDY simulations. In addition, F. Hamann et al. (2019) have clearly shown that LoBAL absorption arises from a highly shielded region in high column density outflows while comparing HiBAL and LoBAL quasars with PV absorption. Here, we develop a model that tests the plausibility of a shielding scenario that may be responsible for the emergence of LoBALs as observed in J1156+0856. In this scenario, the shielding gas absorbs a substantial fraction of the radiation from the accretion disk, thereby changing the photoionization conditions of the gas located farther out. We propose that this shielding can be caused by an additional flow that transits our LOS during epoch 2, as explained in detail below. Note that this may be slightly different from a conventional definition of shielding gas used in the literature before, since we assume that this new flow can also lead to absorption in UV lines.

For our source, we assume that the absorption present in epoch 1 is due to an outflow that is already present along our LOS, say, flow-I. Now, we can also assume that flow-I may not be a single structure, but consists of kinematically separate subcomponents corresponding to the different BAL regions as discussed in Section 3.1. During epoch 2, a new flow having a large column density either emerges near the accretion disk or transits into our LOS at a relatively small distance, referred to hereafter as flow-II. In the following discussion, we use flow-II to represent both scenarios, as their impact on the observed variability, primarily through providing shielding for flow-I, is effectively indistinguishable for the purposes of our analysis.

One of the primary motivations for invoking a multicomponent outflow scenario arises from the distinct absorption properties observed in region E. Nearly all of the Si IV absorption in this region appears during epoch 2, and this can be attributed to the emergence of a new component, i.e., flow-II. Assuming that the roughly flat-bottomed Si IV absorption profile in epoch 2 is a result of saturation, we estimate a covering fraction of $C_{\nu, \text{Si iv}}$ (flow-II) ~ 0.4 , corresponding to the average absorption depth. By contrast, the C IV absorption in region E exhibits a sharp decline in depth, from approximately 0.7 to 0.4, toward higher velocities. This suggests that the average absorption depth, and thus the minimum total covering fraction, is significantly greater for C IV than for Si IV. Furthermore, the average change in C IV absorption depth between epoch 2 (when flow-II is present) and epoch 3 (when it nearly disappears) is also \sim 0.4, closely matching $C_{v,Si}$ iv (flow-II). These findings imply that flow-II is a highly saturated, partially covering absorber in both C IV and Si IV, with $C_v \sim 0.4$. The additional C IV absorption in region E can be attributed to the already existing flow-I, which likely has a higher covering fraction and is superimposed on the saturated profile from flow-II. The disappearance of Si IV absorption in region E by epoch 3 further suggests that flow-I is not contributing to Si IV, indicating either a lower column density or a different ionization state for flow-I at the high velocities. This scenario naturally accounts for the observed discrepancies in covering fractions between C IV and Si IV, supporting the presence of multiple outflow components along the LOS, each with distinct physical properties and temporal

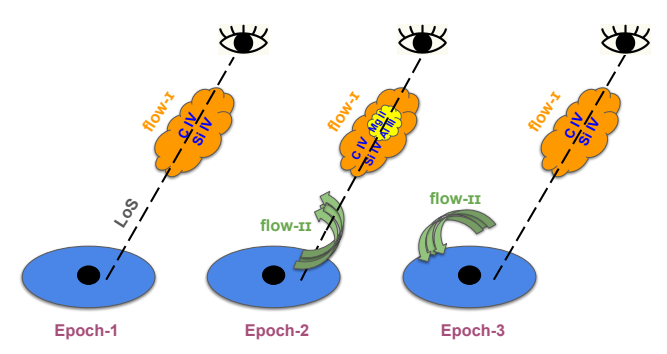


Figure 5. This figure shows a simple schematic diagram of the model of an accretion disk (blue) + two flow components, namely flow-I and flow-II, that we propose in order to explain the BAL variability in J1156+0856. The three panels represent the first three epochs, where flow-I is present in the first epoch, then flow-II enters our LoS in epoch 2, which leads to LoBAL absorption in flow-I and later moves out of the LoS by epoch 3.

behavior. A simple schematic diagram that explains our model is shown in Figure 5 for better clarity.

According to this scenario, the appearance of flow-II in epoch 2 leads to effective shielding of the more distant flow-I from the central ionizing source, resulting in the sudden appearance of low-ionization BALs (LoBALs), such as Al III and Mg II, at velocities corresponding to the strongest C IV absorption. Due to its proximity to the accretion disk, flow-II may move out of our LOS on relatively short timescales (see discussion on transit timescales at the end of this subsection), thereby exposing flow-I once again to unattenuated radiation from the disk. It is also plausible that flow-II may have swept away or disrupted the shielding material near the disk during its passage, further enhancing the exposure of flow-I to highenergy photons. This reexposure could lead to a reduced CIV ion fraction in flow-I, consistent with the weakened absorption observed in epoch 3. However, in epochs 4 and 5, the absorption strengthens and roughly recovers its original profile seen in epoch 1, suggesting that the ionizing flux reaching flow-I may have returned to its earlier state. Interestingly, this period also coincides with the appearance of a distinct, highvelocity absorption component at 26,000–30,000 km s⁻¹. If this new feature is associated with the emergence of another flow launched close to the disk or transits our LOS, it may again provide the shielding necessary for LoBAL formation, potentially leading to the reappearance of LoBAL features in the near future. To test this hypothesis, we plan to continue short-timescale monitoring of this source.

We argue that the proposed multicomponent outflow and a shielding scenario provide a consistent explanation for the observed BAL variability, based on the following points:

- 1. In region D, the Al III absorption does not reappear after epoch 2 (where it initially emerged) even though the corresponding C IV absorption recovers to similar depths in epochs 4 and 5. This behavior is difficult to explain with models invoking ionization changes driven solely by variations in the continuum flux in a single-component outflow. Furthermore, LoBAL features are generally observed at lower velocities, where LOS column densities are expected to be higher (N. Filiz Ak et al. 2014). Hence, their sudden emergence at high velocities is better explained by a shielding scenario.
- 2. Except for epoch 2, the relative absorption depths in the C IV BAL profile remain largely consistent across the

other epochs, indicating that the overall absorption profile is nearly restored to its original shape seen in epoch 1. If the strong variability were primarily driven by large changes in column density—such as those caused by the transiting motion of a single outflowing cloud—it would be highly improbable for the absorption profile to return so closely to its initial state. A similar argument applies to models involving changes in covering fraction alone; such scenarios are unlikely to reproduce the observed profile stability across multiple epochs. These observations again support our interpretation that the variability in flow-I is governed by changes in the shielding gas column density from flow-II rather than by intrinsic changes in the properties of a single outflowing component. However, we acknowledge that some observations remain unexplained by this model. For example, a narrow absorption feature present in region B during epoch 1 disappears in later epochs, suggesting that additional processes, such as localized changes in density, ionization, or cloud structure, may also play a role in shaping the detailed absorption profile.

- 3. The strong anticorrelation between BAL variability and UV-band flux, as discussed in Section 3.3, supports our shielding-based interpretation. Increased shielding reduces high-energy ionizing photons, lowering the ionization parameter and enhancing the C IV fraction. However, the photoionization modeling suggests that the relatively small variations seen in the optical light curves (Figure 4), which trace the low-energy UV continuum in the rest frame, are insufficient to explain the observed BAL changes (P. Aromal et al. 2021). This aligns with our model, where the shielding gas primarily affects the high-energy UV and X-ray continuum that is responsible for BAL variability, while leaving the lower-energy UV flux relatively unchanged.
- 4. The coordinated variability (albeit with varying amplitudes) across the entire velocity range of 6000–30,000 km s⁻¹ suggests a global mechanism influencing flow-I across possibly spatially separated regions of the outflow. This behavior is consistent with a shielding scenario, where changes in the shielding column can simultaneously affect multiple components of the flow.

Lastly, we estimate the typical transit timescale, $\Delta t_{\rm transit} = D_{1500}/v_{\rm transverse}$, where $D_{1500} \sim 0.008$ pc is the characteristic diameter of the continuum-emitting region at 1500 Å (see D. M. Capellupo et al. 2013, for detailed discussion), and $v_{\rm transverse} \sim 20,000~{\rm km~s}^{-1}$ is the assumed transverse velocity of the outflow across the LOS, taken to be comparable to the average outflow velocity observed in J1156+0856. This gives a transit timescale of $\Delta t_{\rm transit} \sim 0.4~{\rm yr}$, which is well within the observed variability timescale of $\Delta t \sim 3~{\rm yr}$ —i.e., the time between epochs 1 and 2, and also between epochs 2 and 3. Hence, these results are consistent with a scenario in which a flow component moves into our LOS and subsequently exits, producing the observed emergence and disappearance of strong absorption features.

4.2. Photoionization Modeling in the Presence of a Shielding Flow

Here we consider our model in Section 4.1 and carry out the photoionization modeling using CLOUDY v23.01 (G. J. Ferland

et al. 2017) simulations. We assume the outflow to be a plane parallel slab with solar metallicity and uniform density illuminated by a quasar spectral energy distribution (SED). Under equilibrium conditions, CLOUDY computes the temperature and ionization states of the absorbing gas.

We consider the mean quasar SED from G. T. Richards et al. (2006; see also P. Aromal et al. 2021), which goes through flow-II, which provides shielding in our model, before reaching flow-I, which is located further away. We perform two CLOUDY runs to test our model. In the first CLOUDY run, the quasar SED is incident on the flow-II located close to the disk (assuming a high-ionization parameter, $log(U) \sim 2$) with the total hydrogen column density (NH,shield) varying from $log(N_{H,shield}) = 22-24.5$ in 0.2 dex steps. Now, if we assume a hydrogen density $log(n_H) = 7$, then flow-II will be placed at a distance of a few subparsecs ($r \sim 0.02 \,\mathrm{pc}$) given $\log(U) \sim 2$. Note that we use this distance as it is similar to the distance estimate one obtains using Keplerian arguments, assuming $v = 10^4 \,\mathrm{km \, s^{-1}}$ and $\log(M_{\rm BH}) = 8.92$ as calculated for J1156 +0856. The specific values of both $\log(U)$ and $n_{\rm H}$ assumed here are not important for our analysis and were chosen in this way so that the distance to the flow-II is in the range of subparsecs, i.e., relatively close to the disk. We note that as $N_{\rm H,shield}$ approaches high values (log($N_{\rm H,shield}$) ~ 23.5), the resulting C IV column density in flow-II itself can produce strong absorption as seen in BALs. Next, we obtain the transmitted continuum after passing through the shielding gas having different $N_{\rm H}$. A comparison between incident and transmitted SED considered here is shown in P. Aromal et al. (2021; Figure 13 therein). The shielding can significantly suppress the flux in the extreme UV and X-ray regimes, thereby substantially altering the ionization conditions in a more distant outflow, i.e., flow-I.

In the second set of CLOUDY runs, we use these transmitted continua as ionizing radiation on an absorber located further away at a distance of a few parsecs, say \sim 5 pc. This corresponds to flow-I in our picture. We modeled this cloud with a total hydrogen column density, $\log(N_{\rm H}) = 18$, having a uniform density $\log(n_{\rm H}) = 7$. We obtain the column density of each ionized species of interest, such as C IV, Si IV, Al III, and Mg II, in flow-I. We call them $N_{\rm shielded,ion}$. We also note these column density values for a different scenario where flow-I is illuminated by a quasar SED without any shielding, i.e., without the presence of flow-II, but located at the same distance as before, say, $N_{\rm ion}$.

distance as before, say, $N_{\rm ion}$. In Figure 6, we plot $\frac{N_{\rm shielded,ion}}{N_{\rm fon}}$ as a function of the column density of shielding gas ($N_{\rm H,shield}$). This shows the effect of shielding gas on the ionic column densities of flow-I. We see that $\frac{N_{\rm shielded,CIV}}{N_{\rm CIV}}$ does not change much with increasing $N_{\rm H,shield}$, whereas low-ionization species like Al III and Mg II show more than an order of magnitude changes as $\log(N_{\rm H,shield})$ approaches 24. This indicates that the column density of low-ionization species is highly sensitive to the shielding gas in between. This may explain the emergence of LoBAL absorption if an outflow is efficiently shielded by a high column density flow close to the disk. Such a scenario is possible, especially during the eruption of a strong wind close to the disk or during the transit of a strong flow component at a relatively smaller distance, as we propose in the case of J1156+0856.

This scenario is similar to the models presented in J. S. Kaastra et al. (2014) and M. Mehdipour et al. (2022).

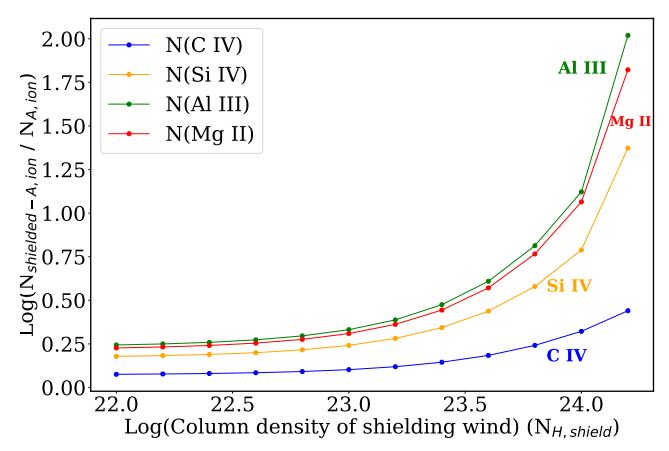


Figure 6. This figure shows the ratio of column density of different ionized species with and without the shielding gas ($N_{\rm shielded,C~IV}$ and $N_{\rm C~IV}$ respectively) as a function of the column density of shielding gas ($N_{\rm H,shield}$).

For example, J. S. Kaastra et al. (2014) observed the emergence of a relatively low-ionization, narrow UV absorption in a previously warm absorber-like outflow in NGC 5548. They concluded that this might be due to the presence of another outflow close to the accretion disk that provides large X-ray obscuration and, at the same time, produces BAL features in the UV spectra (see Figure 4 in J. S. Kaastra et al. 2014). The obscuration decreases the ionization levels in the warm absorber further away, which then appear as relatively low-ionization UV absorption. To make it more interesting, M. Mehdipour et al. (2022) reported that recent observations of NGC 5548 in 2022 indicated a significant reduction in X-ray obscuration and the near disappearance of narrow UV lines mentioned in J. S. Kaastra et al. (2014). Additionally, K. Fukumura et al. (2024) further demonstrated how accretion disk winds can result in both X-ray obscuration and UV absorption lines at the same time using MHD wind models. This picture supports what we propose in the case of J1156 +0856, although we do not find any evidence of X-ray obscuration or X-ray absorption features in J1156+0856 due to X-ray nondetection.

However, the question remains as to why only region D shows low-ionization absorption if the absorption from flow-I is present over a large velocity range. This may be due to density variations along flow-I, as a change in U is highly dependent on the density of the cloud. In this case, region D may be probing a large region of high-density outflowing gas, resulting in a large column density as observed and a relatively smaller U as well. Although our model provides a highly likely scenario, we need more information to confirm the same. In particular, constraining the distance to the outflows necessitates an estimate of their density, which can be derived from alternative methods such as density-sensitive transitions (e.g., S IV). Also, a high-resolution spectrum may help us to resolve the narrow lines in the BAL region, which may provide clues on the extent of saturation and possible kinematic shift in components seen, for example, in BAL region C. Additionally, if our picture holds true, then such an analysis is essential for obtaining the covering fraction of the outflows, which may help us to understand the extent to which multiple outflows can affect each other.

5. Conclusions

We present a detailed analysis of BAL variability in J115633.82+085628.9 using spectroscopic data from the SALT and SDSS, spanning nearly two decades across five epochs. This quasar is part of our high-velocity BAL sample of 63 quasars, which we have been monitoring with SALT for almost a decade (P. Aromal et al. 2023). The BAL in this source spans a wide velocity range from 6700 to $30,000~{\rm km~s^{-1}},$ although the upper limit is a conservative estimate and absorption can extend beyond $30,000~{\rm km~s^{-1}}.$ For clarity, we divide the BAL into five regions, labeled A, B, C, D, and E, corresponding to velocity ranges of $6700-10,000~{\rm km~s^{-1}},$ $10,000-12,500~{\rm km~s^{-1}},$ $12,500-18,000~{\rm km~s^{-1}},$ $18,000-22,000~{\rm km~s^{-1}},$ and $22,000-30,000~{\rm km~s^{-1}},$ respectively.

The C IV BAL exhibits extreme variability throughout our monitoring campaign, including one of the highest EW variation rates ever reported in literature. Notably, we observe the emergence of LoBALs in Al III and Mg II for the first time in epoch 2, coinciding with a significant increase in C IV absorption. These newly appeared LoBALs are found at high velocities (18,000–23,000 km s⁻¹) within region D, where the C IV absorption is also strongest—an unusual location for LoBALs, which are typically found at lower velocities. Interestingly, by epoch 3, the C IV absorption weakens significantly, and the LoBALs completely disappear. This is likely the first instance where the emergence and subsequent disappearance of LoBALs are observed within the same quasar, accompanied by such dramatic C IV changes.

Regions A, B, and C also exhibit significant variability. Region A contains a strong, narrow C IV component with well-resolved Si IV absorption, both showing highly correlated variability. The narrow component in region B disappears completely after epoch 2 and does not reappear in subsequent observations. Region C, in contrast, hosts multiple narrow C IV components, displaying large velocity shifts indicative of kinematic variability. In region E, the C IV absorption depth increases dramatically ($\Delta \sim 0.4$) in epoch 2 relative to epoch 1, while a Si IV absorption with a flat-bottomed profile (indicating saturation) also emerges for the first time, with an average depth of ~ 0.4 .

Motivated by these observations, we propose a two-flow model to explain the observed variability. In this picture, flow-I is a preexisting outflow responsible for the absorption seen in epoch 1. In epoch 2, a new absorbing component, flow-II, with a large column density, emerges close to the accretion disk or transits into our LOS. This additional component provides sufficient shielding to flow-I, leading to the temporary appearance of LoBAL features in region D. As flow-II eventually moves out of the LOS, flow-I is once again exposed to the full ionizing radiation, resulting in the disappearance of the LoBALs. By epochs 4 and 5, the C IV BAL profile roughly returns to its original state from epoch 1. In particular, we did not observe a reappearance of the LoBALs in our subsequent monitoring with SALT.

We also performed simple photoionization modeling using CLOUDY, simulating a multiflow scenario: one component close to the disk (corresponding to flow-II) and a second, more distant component (flow-I). Our models indicate that this configuration can provide sufficient shielding when the column density of flow-II increases and approaches the Compton thickness ($N_{\rm H} \sim 23$ –24). Under such conditions, the LoBAL

column densities become highly sensitive to shielding, which leads to significant changes in optical depth and the emergence of LoBAL features, as observed in epoch 2. There are precedents for this mechanism in the literature. For instance, in NGC 5548, the emergence of an X-ray absorbing BAL outflow was found to coincide with the appearance of new, relatively low-ionization UV absorption features in an already existing outflow component (J. S. Kaastra et al. 2014; N. Arav et al. 2015; M. Mehdipour et al. 2022). In summary, our results suggest that LoBALs sometimes can be transient features in quasars, triggered when substantial shielding is provided to preexisting, distant parts of the outflow, rather than necessarily representing a specific evolutionary phase in quasar lifecycles.

Acknowledgments

This work is supported by the Natural Science and Engineering Research Council (NSERC) RGPIN-2021-04157 and a Western Research Leadership Chair Award. Based on observations collected at Southern African Large Telescope (SALT; Program IDs 2021-2-SCI-008, 2022-2-SCI-005, and 2023-2-SCI-002).

Funding for the Sloan Digital Sky Survey IV has been provided by the Alfred P. Sloan Foundation, the U.S. Department of Energy Office of Science, and the Participating Institutions. SDSS acknowledges support and resources from the Center for High-Performance Computing at the University of Utah. The SDSS website is www.sdss4.org.

SDSS is managed by the Astrophysical Research Consortium for the Participating Institutions of the SDSS Collaboration including the Brazilian Participation Group, the Carnegie Institution for Science, Carnegie Mellon University, Center for Astrophysics | Harvard & Smithsonian (CfA), the Chilean Participation Group, the French Participation Group, Instituto de Astrofisica de Canarias, The Johns Hopkins University, Kavli Institute for the Physics and Mathematics of the Universe (IPMU)/University of Tokyo, the Korean Participation Group, Lawrence Berkeley National Laboratory, Leibniz Institut für Astrophysik Potsdam (AIP), Max-Planck-Institut für Astronomie (MPIA Heidelberg), Max-Planck-Institut für Astrophysik (MPA Garching), Max-Planck-Institut für Extraterrestrische Physik (MPE), National Astronomical Observatories of China, New Mexico State University, New York University, University of Notre Dame, Observatório Nacional/MCTI, The Ohio State University, Pennsylvania State University, Shanghai Astronomical Observatory, United Kingdom Participation Group, Universidad Nacional Autónoma de México, University of Arizona, University of Colorado Boulder, University of Oxford, University of Portsmouth, University of Utah, University of Virginia, University of Washington, University of Wisconsin, Vanderbilt University, and Yale University.

Data Availability

Data used in this work are obtained using SALT. Raw data will become available for public use 1.5 yr after the observing date at https://ssda.saao.ac.za/.

Software: astropy (Astropy Collaboration et al. 2022), Cloudy (G. J. Ferland et al. 2017), PYQSOFIT (H. Guo et al. 2018)

ORCID iDs

P. Aromal https://orcid.org/0009-0001-2178-4022
R. Srianand https://orcid.org/0000-0002-9062-1921
S. C. Gallagher https://orcid.org/0000-0001-6217-8101
M. Vivek https://orcid.org/0000-0001-5937-331X

References

```
Ahmed, H., Shemmer, O., Matthews, B., et al. 2024, ApJ, 968, 77
Allen, J. T., Hewett, P. C., Maddox, N., Richards, G. T., & Belokurov, V.
   2011, MNRAS, 410, 860
Arav, N., Liu, G., Xu, X., et al. 2018, ApJ, 857, 60
Arav, N., Chamberlain, C., Kriss, G. A., et al. 2015, A&A, 577, A37
Aromal, P., Srianand, R., & Petitjean, P. 2021, MNRAS, 504, 5975
Aromal, P., Srianand, R., & Petitjean, P. 2022, MNRAS, 514, 1975
Aromal, P., Srianand, R., & Petitjean, P. 2023, MNRAS, 522, 6374
Aromal, P., Srianand, R., & Petitjean, P. 2024, MNRAS, 527, 12298
Astropy Collaboration, Price-Whelan, A. M., Lim, P. L., et al. 2022, ApJ,
Bellm, E. C., Kulkarni, S. R., Barlow, T., et al. 2019a, PASP, 131, 068003
Bellm, E. C., Kulkarni, S. R., Graham, M. J., et al. 2019b, PASP, 131, 018002
Burgh, E. B., Nordsieck, K. H., Kobulnicky, H. A., et al. 2003, Proc. SPIE,
   4841, 1463
Capellupo, D. M., Hamann, F., Shields, J. C., Halpern, J. P., & Barlow, T. A.
   2013, MNRAS, 429, 1872
Capellupo, D. M., Hamann, F., Shields, J. C., Rodríguez Hidalgo, P., &
   Barlow, T. A. 2011, MNRAS, 413, 908
Capellupo, D. M., Hamann, F., Shields, J. C., Rodríguez Hidalgo, P., &
   Barlow, T. A. 2012, MNRAS, 422, 3249
Chambers, K. C., Magnier, E. A., Metcalfe, N., et al. 2016, arXiv:1612.05560
Choi, H., Leighly, K. M., Terndrup, D. M., et al. 2022, ApJ, 937, 74
Dai, X., Shankar, F., & Sivakoff, G. R. 2008, ApJ, 672, 108
De Cicco, D., Brandt, W. N., Grier, C. J., et al. 2018, A&A, 616, A114
Ferland, G. J., Chatzikos, M., Guzmán, F., et al. 2017, RMxAA, 53, 385
Filiz Ak, N., Brandt, W. N., Hall, P. B., et al. 2012, ApJ, 757, 114
Filiz Ak, N., Brandt, W. N., Hall, P. B., et al. 2013, ApJ, 777, 168
Filiz Ak, N., Brandt, W. N., Hall, P. B., et al. 2014, ApJ, 791, 88
Fukumura, K., Mehdipour, M., Behar, E., et al. 2024, ApJ, 968, 70
Gibson, R. R., Brandt, W. N., Gallagher, S. C., Hewett, P. C., &
   Schneider, D. P. 2010, ApJ, 713, 220
```

```
Gibson, R. R., Brandt, W. N., Schneider, D. P., & Gallagher, S. C. 2008, ApJ,
  675, 985
Green, K. S., Gallagher, S. C., Leighly, K. M., et al. 2023, ApJ, 953, 186
Grier, C. J., Hall, P. B., Brandt, W. N., et al. 2015, ApJ, 806, 111
Guo, H., Shen, Y., & Wang, S., 2018 PyQSOFit: Python Code to Fit the
  Spectrum of Quasars, Astrophysics Source Code Library, ascl: 1809.008
Hamann, F., Herbst, H., Paris, I., & Capellupo, D. 2019, MNRAS, 483, 1808
Kaastra, J. S., Kriss, G. A., Cappi, M., et al. 2014, Sci, 345, 64
Kobulnicky, H. A., Nordsieck, K. H., Burgh, E. B., et al. 2003, Proc. SPIE,
  4841, 1634
Law, N. M., Kulkarni, S. R., Dekany, R. G., et al. 2009, PASP, 121, 1395
Leighly, K. M., Terndrup, D. M., Gallagher, S. C., Richards, G. T., &
  Dietrich, M. 2018, ApJ, 866, 7
Lu, W.-J., & Lin, Y.-R. 2020, MNRAS, 499, L58
Lu, W.-J., & Lin, Y.-R. 2025, ApJ, 985, 93
Lyke, B. W., Higley, A. N., McLane, J. N., et al. 2020, ApJS, 250, 8
McGraw, S. M., Brandt, W. N., Grier, C. J., et al. 2017, MNRAS, 469, 3163
McGraw, S. M., Shields, J. C., Hamann, F. W., et al. 2015, MNRAS,
  453, 1379
Mehdipour, M., Kriss, G. A., Costantini, E., et al. 2022, ApJL, 934, L24
Mishra, S., Vivek, M., Chand, H., & Joshi, R. 2021, MNRAS, 504, 3187
Murray, N., Chiang, J., Grossman, S. A., & Voit, G. M. 1995, ApJ, 451, 498
Rankine, A. L., Hewett, P. C., Banerji, M., & Richards, G. T. 2020, MNRAS,
  492, 4553
Richards, G. T., Lacy, M., Storrie-Lombardi, L. J., et al. 2006, ApJS, 166, 470
Rogerson, J. A., Hall, P. B., Ahmed, N. S., et al. 2018, ApJ, 862, 22
Srianand, R., & Petitjean, P. 2001, A&A, 373, 816
Temple, M. J., Rankine, A. L., Banerji, M., et al. 2024, MNRAS, 532,
Urrutia, T., Becker, R. H., White, R. L., et al. 2009, ApJ, 698, 1095
Vilkoviskij, E. Y., & Irwin, M. J. 2001, MNRAS, 321, 4
Vivek, M. 2019, MNRAS, 486, 2379
Vivek, M., Srianand, R., & Dawson, K. S. 2018, MNRAS, 481, 5570
Vivek, M., Srianand, R., Mahabal, A., & Kuriakose, V. C. 2012, MNRAS,
  421, L107
Vivek, M., Srianand, R., Petitjean, P., et al. 2014, MNRAS, 440, 799
Wang, T., Yang, C., Wang, H., & Ferland, G. 2015, ApJ, 814, 150
Weymann, R. J., Morris, S. L., Foltz, C. B., & Hewett, P. C. 1991, ApJ,
Wu, L., Wang, J.-X., Ren, W.-K., & Kang, W.-Y. 2024, MNRAS, 533, 908
Yi, W., Brandt, W. N., Hall, P. B., et al. 2019, ApJS, 242, 28
Yi, W., & Timlin, J. 2021, ApJS, 255, 12
```